RSC Advances

ROYAL SOCIETY OF CHEMISTRY

www.rsc.org/advances

Ultra-thin coating of g-C_3N_4 on an aligned ZnO nanorod film for rapid charge separation and improved photodegradation performance

Tae Joon Park,[a] Rajendra C. Pawar,[b] Suhee Kang[b] and Caroline Sunyong Lee*[b]

[a] Research Institute of Engineering and Technology, Hanyang University, 55 Hanyangdaehak-ro, Sangrok-gu, Ansan-si, Gyeonggi-do 426-791, Republic of Korea

[b] Department of Materials Engineering, Hanyang University, 55 Hanyangdaehak-ro, Sangrok-gu, Ansan-si, Gyeonggi-do 426-791, Republic of Korea

Correspondence should be addressed to Caroline Sunyong Lee; sunyonglee@hanyang.ac.kr

Abstract

Type II heterogeneous films with one dimensional (1D) zinc oxide (ZnO) nanorods coated with the graphitic carbon nitride (g-C_3N_4) layer (1D ZnO/gC_3N_4) were fabricated by a simple reflux and thermal vapor condensation process. The grown 1D ZnO/gC_3N_4 films were used to degrade methylene blue (MB) dye under visible-light irradiation. Additionally, photoelectrochemical (PEC) measurements were conducted to explore charge separation and transportation processes. The fabricated films had a photocurrent density of 0.12 mA cm^{-2}, which is 3.7-times higher than that of bare ZnO nanorods, and had good stability over 5 h. Moreover, the photocatalytic activities of ZnO with the g-C_3N_4 films performed well over multiple cycles without requiring a complex washing process for the photocatalytic recovery step. The improved performance stemmed from direct coating of an ultra-thin g-C_3N_4 layer (< 10 nm thick) over ZnO nanorods, which induced high optical absorbance in the visible range, effective charge separation and transportation and low interfacial charge transfer resistance. A photodegradation mechanism was proposed based on the generation of $OH^{\bullet}$ and hole radicals during MB dye degradation; these

radicals were verified using *tert*-butanol and EDTA-2Na scavengers. The fabricated core–shell films are very promising components for PEC devices for water purification applications.

Introduction

Increasing water pollution is one of the greatest challenges to the environment. Photocatalysis using inexhaustible solar energy has been extensively studied as a way to degrade wastewater.[1] A wide variety of inorganic materials, especially metal oxides, have been explored as photocatalysts for wastewater purification under UV or visible-light irradiation.[2-4] Zinc oxide (ZnO), one of the most widely researched metal oxide semiconductors, shows superior electron transfer performance,[5] providing photogenerated holes for strong oxidation, and is inexpensive and non-toxic.[6] However, two critical drawbacks of ZnO are its limited response to UV-light irradiation because of its 3.2-eV bandgap and its high probability of recombination of photogenerated electron-hole pairs. There have been many attempts to overcome these limitations, such as doping,[7-12] decorating metals[13-16] and combining with other semiconductors.[17-21] Furthermore, nanostructural engineering has provided a way to enhance the performance of some photocatalytic materials.[22] Aligned one-dimensional nanostructures have improved charge carrier transfer because they provide a direct path for carrier transportation and collection along their length.[23,24] The recombination of photogenerated charge carriers is reduced, thereby resulting in enhanced performance of the photocatalytic materials.

Graphitic carbon nitride (g-C_3N_4), a metal-free conjugated polymeric semiconductor, is composed of stacks of two-dimensional layers with tri-s-triazine building block connections within each layer and van der Waals forces acting between the layers.[25] g-C_3N_4 is fabricated using a straightforward process involving low-temperature thermal condensation of nitrogen-rich starting materials such as melamine, dicyandiamide and thiourea. Its desirable characteristics, which include cost-effectiveness, high chemical stability and a relatively narrow bandgap of 2.7 eV, make g-C_3N_4 useful in photoelectrochemical (PEC) applications such as the degradation of organic pollutants under visible-light irradiation and water splitting to produce hydrogen using solar energy.[26-30] However, g-C_3N_4 has its limitations, just like other photocatalysts, e.g., low quantum yield and high recombination of photogenerated charge carriers.

To overcome these issues, ZnO and g-C_3N_4 were combined to make heterostructured powders having enhanced charge carrier separation and transfer.[31-35] Such ZnO@g-C_3N_4 hybrid photocatalysts, made by a mechanical milling method, showed enhanced photocatalytic activities compared with single-phase g-C_3N_4.[36] The low temperature sonication method has been

employed to make nitrogen doped ZnO/g-C_3N_4 nanoplates and exhibited better performance compared to their pristine structures.[37] The mesoporous g-C_3N_4 structure has been synthesized via hard template method, and then combined with ZnO particles with sonication and sintering processes for the remarkable visible light photocatalytic activity.[38] Several g-C_3N_4/ZnO nanocomposites have been prepared by a calcination approach and evaluated toward methylene blue (MB) photodegradation.[39,40] The synthesis and photocatalytic behavior of dumbbell- and cone-shaped ZnO, prepared using hydrolyzing agents and chemisorbed on bulk g-C_3N_4, have been reported.[41] However, this approach is time-consuming and cost-inefficient; furthermore, it is associated with particular difficulty in controlling for hierarchical micro-nanostructures, resulting not only in poor adhesion between ZnO and g-C_3N_4, but also poor photocatalytic activity and relatively low stability. Similar reference is reported using electrochemical deposition method to fabricate ZnO nanorods with thin g-C_3N_4 layer. However, critical drawbacks of this method are high cost, a cause of environmental concern because of the toxic reaction residue.[42] Repeated recyclability is required to produce photocatalysts at low cost. Because of the fine morphology of photocatalyst nanoparticles, sophisticated processes, such as centrifugation and sonication-assisted dispersion and drying, are extensively used during the recovery process after photocatalytic reactions. A crucial disadvantage of this recovery process is the significant weight loss of the photocatalyst nanoparticles. Thus, it is important to develop highly stable, recyclable and micro-nanostructured ZnO/g-C_3N_4 photocatalysts with enhanced optical and electrical properties in a simple and cost-effective manner.

We report herein a simple method to fabricate heterostructured 1D ZnO/gC_3N_4 films that leverage the superior electron transport properties of vertically-aligned one-dimensional ZnO nanorods with the visible-light absorption properties of the g-C_3N_4 layer. The method uses simple refluxing with thermal vapor condensation. Compared to bare ZnO nanorods, 1D ZnO/gC_3N_4 films exhibited superior PEC performance with high photocurrent densities and low charge carrier transfer resistances. Consequently, these core–shell films would likely show fast, reusable and stable photodegradation of organic pollutants. Finally, the core–shell films were readily recycled using only purified water and maintained their photocatalytic activities for consecutive photodegradation of MB dye solutions.

2 Experimental section

2.1 Materials

Zinc acetate dihydrate ($Zn(CH_3COO)_2{\cdot}2H_2O$) and melamine (2,4,6-triamino-1,3,5-triazine) were purchased from Junsei Chemical Co. (Tokyo, Japan). Hexamethylenetetramine ($C_6H_{12}N_4$, HMTA) was purchased from Daejung Chemicals & Metals Co. (Daejung, Korea). Absolute ethanol was purchased from Merck KGaA, Darmstadt, Germany). Purified water was used throughout the work. Fluorine-doped tin oxide (FTO)-coated glass of dimensions 2×6 cm^2 was obtained from Hanalintech (Yongin, Korea).

2.2 Preparation of 1D ZnO/gC3N4 films

Vertically-aligned ZnO nanorods were fabricated on FTO-coated glass substrates by seed-mediated growth, as reported previously.[43-45] Briefly, seed films of ZnO were prepared by dipping the substrates into zinc acetate dihydrate solutions (0.05 M in absolute ethanol) for 20 s and maintaining at room temperature for 12 h to evaporate the solvents. The as-prepared films were annealed at 400°C for 5 min in air. The seed films of ZnO were then placed vertically in an aqueous solution consisting of zinc acetate dihydrate (0.05 M) and HMTA (0.05 M), and the solution was refluxed at 95°C for 5 h. The resulting substrates coated with ZnO nanorods were washed several times and oven-dried. Melamine (0.5 g) and the as-prepared vertically-aligned ZnO nanorods were place in a crucible. The covered crucibles were placed in a muffle furnace in an air atmosphere and heated at a rate of 10 °C/min to 520°C, which was maintained for 4 h. The 1D ZnO/gC_3N_4 films are described as 1D ZnO/gC_3N_4 _1, 2 and 3 (corresponding to the different amounts of melamine, i.e., 0.125, 0.5 and 1.0 g, respectively) throughout this paper.

2.3 Characterization

Surface and cross-sectioned structures of the 1D ZnO/gC_3N_4 films were analyzed using a field-emission scanning electron microscope (FE-SEM) (model SU70, 5 kV; Hitachi, Tokyo, Japan) equipped with an energy-dispersive X-ray spectrometer (EDS). A high-resolution transmission electron microscope (HR-TEM) (model JEM–2010F, 200 kV; JEOL, Tokyo, Japan) was also

used to study the samples. X-ray diffractometer (XRD) was used to confirm the crystallinity and orientation (Rigaku, D/MAX-2500/PC Cu Kα line, USA). Fourier transform infrared (FT-IR) spectra were recorded on a Bruker IFS 66/S instrument (Bruker, Billerica, MA, USA) using attenuated total reflection (ATR). X-ray photoelectron spectroscopic (XPS) (Sigma Probe, Thermo-Scientific, Waltham, MA, USA) analyses were conducted *in vacuo* using a multichannel electron spectrometer. A VersaSTAT 4 potentiostat (Princeton Applied Research, Princeton, NJ, USA) was used for the PEC measurements in a standard three-electrode arrangement using the ZnO nanorods on FTO, 1D ZnO/gC_3N_4 films on FTO, graphite and an Ag/AgCl as the working, counter and reference electrodes, respectively. The aqueous electrolyte was 0.5 M Na_2SO_4 (pH = 6.8). All PEC measurements were conducted under visible irradiation. Linear sweep voltammetry (LSV) was performed at a voltage scan rate of 10 mV s^{-1}. Chronoamperometric curves were obtained at 1.0 V versus the reversible hydrogen electrode (RHE). Electrochemical impedance spectroscopy (EIS) measurement was performed using an AC amplitude of 10 mV in the frequency range of 1 Hz to 1,000 kHz. Absorbance spectra of the core–shell films were recorded using a V–600 ultraviolet–visible (UV-Vis) spectrophotometer (Jasco, Tokyo, Japan).

2.4 Photocatalytic activity

The photocatalytic activities of the 1D ZnO/gC_3N_4 films were assessed by the photodegradation of MB under visible light as a function of the irradiation time. As-prepared samples were immersed into a 1×10^{-5} M MB solution and stirred at room temperature. The source of visible light was a 100 W halogen lamp (Il-Kwang Co., Ltd, South Korea with the range of 400 to 900 nm).[46] Analytical solutions (3 mL) were collected from the reaction vessel every 30 min and monitored by the optical absorbance peak at 664 nm. After photocatalytic reaction measurements, the 1D ZnO/gC_3N_4 films were immersed in purified water for 150 min to remove dye molecules and byproducts and dried in an oven at 60°C. Then the washed samples were again placed into the MB solution to confirm the recyclability. Two scavengers, 10 mM *tert*-butanol (t-BuOH) and 10 mM ethylenediaminetetraacetic acid disodium salt (EDTA-2Na), were added during the photocatalytic reactions.

Results and discussion

The two-step fabrication process of the 1D ZnO/gC_3N_4 films is illustrated in Figure 1. Briefly, ZnO nanorods were grown vertically on an FTO-coated glass substrate by seed-mediated growth. These vertically-aligned ZnO nanorod films were placed in the middle of a crucible containing melamine as the g-C_3N_4 source; the amount of melamine was varied. Treatment by thermal vapor condensation at 520°C induced polymerization of the melamine and resulted in a thin g-C_3N_4 layer covering the surface of the ZnO nanorods.[47,48] FE-SEM images revealing the different surface morphologies and cross-sectional structures are shown in Figure 2a and c shows that the ZnO nanorods grew uniformly and vertically on the FTO-coated substrate and had an average length of about 2.5 μm and an average diameter of 180 nm. The diameter of the nanorods increased slightly after the deposition of the g-C_3N_4 layer, which indicated that the 1D ZnO/gC_3N_4 structures were successfully fabricated (Figure 2b and d). As increase the amount of melamine precursors, g-C_3N_4 loaded onto the ZnO nanorods gradually (Figure S1). It can be seen that ZnO nanorods with several g-C_3N_4 nanoparticles (Figure S1a) and g-C_3N_4 layer covered onto ZnO nanorods when the critical amount of melamine was used (Figure S2b). But g-C_3N_4 particles were agglomerated and stacked on the top of ZnO nanorods (Figure S2c). It can lead to increase visible light absorption properties and enhance photocatalytic activities. If the amount of melamine precursors is too high, an excessive g-C_3N_4 loaded can cause the aggregation of g-C_3N_4. It causes incensement of the recombination of photo-generated charge carriers because it have to diffuse longer to reach the interface between ZnO and g-C_3N_4 to collect separately. EDS elemental mapping (Figure 2e) was used to identify the element distributions in the 1D ZnO/gC_3N_4 structures; Zn, O, C and N were observed across the cross-sectional area (Figure 2d). TEM and HR-TEM images (Figure 3) provided detailed information concerning the microstructures; the diameter of the bare ZnO nanorods was ca. 180 nm (Figure 3a) and its selected area electron diffraction (SAED) pattern indicated that it was a single crystal structure (inset of Figure 3(a)). The adjacent lattice fringes of crystalline ZnO and its distance in the [0001] direction of the growth of ZnO nanorod was calculated to be about 0.26 nm, matching to the interplanar distance of the (0002) plane of the ZnO crystals (Figure 3b). The HR-TEM image (Figure 3c) shows the 1D ZnO/gC_3N_4 structures and the g-C_3N_4 shell layer composed of an irregular sheet. The surface of the ZnO nanorods was coated with a thin g-C_3N_4 layer. The

formed heterojunction structures could enhance charge carrier transfer and separation of photoelectrons and could show better photocatalytic activities.

XRD patterns show its crystal phase properties of ZnO nanorods, pure g-C_3N_4 and the 1D ZnO/gC3N4 films as a function of melamine amount (Figure S2). The pronounced diffraction peaks of ZnO nanorods located at 31.79, 34.42, 36.25, 47.44 and 56.53 °, correspond to (100), (002), (101), (102) and (110) planes, respectively. All the peaks can be indexed as the wurtzite phase (JCPDS 36−14151). In case of pure g-C_3N_4, the two main diffraction peaks at 13.1 and 27.5 °, corresponds to the (100) and (002) planes respectively. The weaker peak at (100) plane is attributed to interlayer stacking of aromatic rings for graphitic materials and the stronger peak at (002) plane can be ascribed to the interlayer distance on the g-C_3N_4. However, specific diffraction peaks for g-C_3N_4 was not observed in the 1D ZnO/gC_3N_4 films. The absence of this diffraction peaks can be ascribed to the reason that the amount of g-C_3N_4 was very low and well dispersed onto the ZnO nanorods.

FT-IR spectrum were analyzed to confirm the presence of g-C_3N_4 functional groups. The spectrum of the pure g-C_3N_4 showed strong bands at 810 and 1,200–1,700 cm^{-1} region (Figure 4a), which corresponded to the breathing vibration mode of the tri-s-triazine ring and the stretching mode of the aromatic C–N ring.[30] The broad peaks were ascribed to the vibration modes of the hydroxyl group of adsorbed water. The characteristic functional peaks of the 1D ZnO/gC_3N_4 films resembled those of pure g-C_3N_4, indicating that the g-C_3N_4 layer was well-coated on the ZnO nanorods.

XPS was used to determine the elemental compositions and the molecular bonding information of the core–shell films. The major peaks corresponded to those of Zn, O, C and N (Figure 4b). The binding energy peak positions appeared at 1,021.32 and 1,044.42 eV, corresponding to the spin-orbit splitting of the Zn $2p_{1/2}$ and the Zn $2p_{3/2}$ energy levels (Figure 4c).[49] The high-resolution XPS O 1s spectrum (Figure 4d) shows three peaks centered at 529.98, 531.37 and 532.47 eV. The weak peak at 529.98 eV corresponded to chemisorbed oxygen and the two peaks at 531.37 and 532.47 eV were attributed to oxygen-deficient regions of the ZnO nanorods and lattice oxygen, respectively.[50,51] The three peaks in the high-resolution C 1s XPS spectrum (Figure 4e), centered at 284.60, 286.17 and 288.17 eV, were assigned to sp^2-hybridized C–C

bonds, sp^3-bonded carbon of defects on the g-C_3N_4 surface and N-containing aromatic rings (N–C=N), respectively. The high-resolution N 1s XPS spectrum (Figure 4f) showed a weak peak at 400.02 eV, which was ascribed to tertiary nitrogen N–$(C)_3$ groups and another peak at 398.77 eV, which was assigned to sp^2-hybridized nitrogen atoms in the triazine heterocyclic rings.[52] These results confirmed the formation of a g-C_3N_4 layer on the ZnO nanorods.

PEC measurements were conducted to further explore the electrochemical properties of the ZnO nanorod film, g-C_3N_4 films and the 1D ZnO/gC_3N_4 films (Figures 5 and S1). A linear potential sweep voltammetry plot from –0.4 to 0.9 V was obtained for the photoelectrodes. The photocurrent density of 1D ZnO/gC_3N_4_2 was higher than those of 1D ZnO/gC_3N_4_1 and 1D ZnO/gC_3N_4_3 (Figure S1a). The photocurrent response of the photoelectrodes was tested under visible- light irradiation. A rapid photocurrent response was obtained, with the 1D ZnO/gC_3N_4_2 electrode exhibiting the highest photocurrent density of 0.12 mA cm^{-2} (Figures 5b and S1b). The 1D ZnO/gC_3N_4 films showed higher photocurrent densities than that of the ZnO nanorod film and g-C_3N_4 films because of the excellent visible-light absorption of g-C_3N_4, and because the junction between the ZnO nanorods and the g-C_3N_4 layer enabled efficient separation and transfer of charge carriers. The photocurrent density remained stable throughout 5 h of continuous visible-light irradiation (Figure 6).

EIS is a powerful tool for characterizing charge carrier transport properties and separation. EIS measurements were studied to support the above results and elucidate the separation and transfer of the charge carriers (Figures 5 and S1). The diameter of the arc of a Nyquist plot shows the charge carrier transport resistance between the photoelectrode and the electrolyte. The arc diameter for the 1D ZnO/gC_3N_4 films were smaller than that for the ZnO nanorod film and g-C_3N_4 films, both in the dark and under visible-light irradiation, which indicated a lower charge carrier transport resistance at the photoelectrode/electrolyte interface (Figure 5c and d). The g-C_3N_4 layer on the ZnO nanorod film had facilitated charge carrier transfer and separation because of the type II heterostructure between the ZnO nanorods and the g-C_3N_4 layer.

Based on the results shown above, it was found that the 1D ZnO/gC_3N_4 films hold promise for photocatalytic applications such as the photodegradation of organic dye molecules. The optical absorption and bandgap structure of a photocatalyst are important determinants of its

photocatalytic activity. Figure S2a shows the absorption spectra of the samples as a function of melamine amount. The ZnO nanorods exhibited intense absorption in the UV region with the absorption edge at about 380 nm and the absorption edge of g-C_3N_4 is about 460 nm. Increasing the melamine amount caused the absorption range of the 1D ZnO/gC_3N_4 films to gradually extend because of the visible light absorption properties of g-C_3N_4 layers.[36,53] The bandgap of samples can be calculated through a plot of the Kubelka−Munk function (Figure S2b). The bandgaps of 1D ZnO nanorods and g-C_3N_4 are found to be 3.19 and 2.68 eV, respectively and that of 1D ZnO/gC_3N_4 films are located between them. Therefore, introducing a g-C_3N_4 layer on the ZnO nanorods improved the visible-light activity of the film; a lower bandgap is advantageous to create charge carriers and thereby enhance photocatalytic activity.

The photocatalytic activities of the 1D ZnO/gC_3N_4 films were followed by the degradation of MB at λ = 664 nm under visible-light irradiation. Gentle stirring was used to generate a mild water flow during the entire degradation experiment. Figure S3 shows the changes that occurred in the absorption spectrum during MB photodegradation using the different photocatalysts. MB dye has rapidly degraded in the presence of the 1D ZnO/gC_3N_4 films than with the ZnO nanorod film or g-C_3N_4 films only because of its improved bandgap alignment, and charge carrier separation and transfer. Although bare ZnO nanorods did not exhibit significant visible light absorption, it can degrade MB dye solution under visible light irradiations because of the presence of surface defects on ZnO nanorods. The defects which were created by self-doping on the 1D ZnO nanorods, can create unoccupied states in the forbidden gap. These defects act as an electron receiver and the electrons in the VB can be excited to unoccupied states.[54,55] The normalized absorption ratio (A/A_0) of MB followed the Beer–Lambert law and was directly proportional to the actual concentration.[56,57] Figure 7a shows that the ZnO nanorod film and g-C_3N_4 films degraded only 15% and 39% of the MB dye after 60 min. of exposure, respectively. The 1D ZnO/gC_3N_4 films, which are a combination of two semiconductors, showed the highest photocatalytic activity with 98% of the MB dye degrading after 60 min. The photocatalytic degradation with the 1D ZnO/gC_3N_4 films followed pseudo-first order kinetics, and the kinetic rate constant of photodegradation (κ) was calculated.[58] The photocatalytic performance of the 1D ZnO/gC_3N_4 films ($\kappa = 41.21 \times 10^{-3}$ min^{-1}) was higher than that of the blank solution ($\kappa = 0.70 \times 10^{-3}$ min^{-1}), the ZnO nanorod film ($\kappa = 2.65 \times 10^{-3}$ min^{-1}) and g-C_3N_4 films ($\kappa = 6.87 \times 10^{-3}$

min^{-1}) (Figure 7b), which indicated that the introduction of g-C_3N_4 layer onto ZnO nanorod film enhanced the photocatalytic activity of the bare ZnO nanorods because of its improved charge carrier generation, separation and transfer. The recyclability of the 1D ZnO/gC_3N_4_2 film was also studied under visible-light irradiation. Briefly, the core–shell films were immersed into the MB solution to adsorb dye molecules and were then irradiated with the light source for 150 min to degrade the MB dye. After the first cycle, the films were removed from the reaction vessel and immersed in purified water with gentle stirring for 2 h to remove any residual dye or degradation products. Then, the films were transferred into a new reaction vessel for the recycle test. The photocatalytic activities of the core–shell films toward MB dye under visible-light irradiation remained stable even after four cycles (Figure 7c). The degradation efficiency increased slightly after the first cycle. After 1st cycle, the weight of 1D ZnO/gC_3N_4 films has decreased by 0.02 % compared with the one before any cycle. However, there was no change in weight after second cycle measurement (Figure S6). This may have been due to detachment of loosely bound g-C_3N_4 nanoparticles from the surfaces of 1D ZnO/gC_3N_4 films during the first cycle, which increased the reactive surface area and thereby the degradation efficiency during subsequent cycles.[59] Overall, the core–shell films were easily recycled without using sophisticated processes such as centrifugation or sonication. The unique 1D ZnO/gC_3N_4 structure, with its high chemical stability, enabled the maintenance of high photocatalytic activity. Radical capturing experiments were also conducted to identify the possible photocatalytic reaction mechanism of the 1D ZnO/gC_3N_4 films. The organic MB dye was degraded by the photogenerated radicals. Two radical scavengers, t-BuOH as a hydroxyl radical ($OH^{\bullet}$) scavenger and EDTA-2Na as a hole radical scavenger, were selected to investigate the role of radicals in the photocatalytic degradation of MB. Figure 7d shows that the photocatalytic activity of the core–shell films in the absence of scavengers was about 98% efficient. In contrast, the photocatalytic activities of the 1D ZnO/gC_3N_4 films in the presence of EDTA-2Na and t-BuOH were lower at 39.8 and 51.2%, respectively. This indicated that $OH^{\bullet}$ and hole radicals were the main reactive species in the photodegradation of MB. These findings were used to develop the photocatalytic reaction mechanism of the 1D ZnO/gC_3N_4 films shown in Figure 8. The g-C_3N_4 layer was excited under visible-light irradiation and generated electrons in the conduction band (CB). Excited electrons were readily transferred from the CB of the g-C_3N_4 layer to the CB of the ZnO because the ZnO CB edge position is lower than that of the g-C_3N_4 layer; holes generated in the ZnO valence band

(VB) were transferred to the g-C_3N_4 layer. Therefore, an internal electrostatic potential field was generated at the junction of the core–shell structure, which led to accelerated separation of the charge carriers. The charge carriers subsequently moved to the surface of the 1D ZnO/gC_3N_4 photocatalyst and reacted with dissolved oxygen and water to produce active radicals, or reacted with MB dye directly.

Conclusions

We developed 1D ZnO/gC_3N_4 films having enhanced PEC performances and photocatalytic activities under visible-light irradiation. ZnO nanorods provided a direct channel for electron transfer, and the g-C_3N_4 layer was deposited on vertically-aligned ZnO nanorods by thermal vapor condensation, increasing the visible-light absorption compared to bare ZnO nanorods. Type II heterostructures formed between the ZnO nanorods and the g-C_3N_4 layer, which effectively separated the photoexcited charge carriers and reduced charge recombination. Based on the results of visible-light photodegradation of MB dye, the photocatalytic activity of 1D ZnO/gC_3N_4 films was 20-times faster than that of the bare ZnO nanorods. After the photocatalytic reaction, the core–shell film could be recycled by simply washing with purified water. The photocatalytic performance remained stable even after four cycles. The synthesized 1D ZnO/gC_3N_4 films show great potential for a broad range of applications, such as environmental remediation and solar-driven water splitting.

Acknowledgments

This work was supported by the Energy Efficiency and Resources Core Technology Program of the Korean Institute of Energy Technology Evaluation and Planning (KETEP), and granted financial resources from the Ministry of Trade, Industry and Energy, Republic of Korea (No. 20142020103730), by the Industrial Technology Innovation Program of the Korea Evaluation Institute of Industrial Technology (KEIT) granted financial resource from the Ministry of Trade, Industry & Energy, Republic of Korea. (No. 10062510), and the Human Resources Development

program (No. 20154030200680) of the Korean Institute of Energy Technology Evaluation and Planning (KETEP) grant (funded by the Ministry of Trade, Industry and Energy).

References

[1] X. Yu, A. Shavel, X. An, Z. Luo, M. Ibáñez, A. Cabot, *J. Am. Chem. Soc.* 2014, **136**, 9236−9239.

[2] D. Chen, S. Ouyang, J. Ye, *Nanoscale Res Lett* 2009, **4**, 274−280.

[3] T. Abe, M. Kaneko, *Prog. Polym. Sci.* 2003, **28**, 1441–1488.

[4] G. Shen, P. Chen, K. Ryu, C. Zhou, *J. Mater. Chem.* 2009, **19**, 828–839.

[5] D. G. Schlom, L. N. Pfeiffer, *Nat. Mater.* 2010, **9**, 881–883.

[6] T. Wang, B. Jin, Z. Jiao, G. Lu, J. Ye, Y. Bi, *Chem. Commun.* 2015, **51**, 2103–2106.

[7] X. Yang, A. Wolcott, G. Wang, A. Sobo, R. C. Fitzmorris, F. Qian, J. Z. Zhang, Y. Li, *Nano Lett.* 2009, **9**, 2331–2336.

[8] V. Etacheri, R. Roshan, V. Kumar, *ACS Appl. Mater. Interfaces* 2012, **4**, 2717−2725.

[9] S. Anandan, M. Miyauchi, *Phys. Chem. Chem. Phys.* 2011, **13**, 14937–14945.

[10] F. Barka-Bouaifel, B. Sieber, N. Bezzi, J. Benner, P. Roussel, L. Boussekey, S. Szuneritsa, R. Boukherroub, *J. Mater. Chem.* 2011, **21**, 10982–10989.

[11] J. Huo, L. Fang, Y. Lei, G. Zenga, H. Zeng, *J. Mater. Chem. A* 2014, **2**, 11040–11044.

[12] H. Ma, L. Yue, C. Yu, X. Dong, X. Zhang, M. Xue, X. Zhang, Y. Fu, *J. Mater. Chem.* 2012, **22**, 23780–23788.

[13] W. L. Ong, S. Natarajan, B. Kloostra, G. W. Ho, *Nanoscale* 2013, **5**, 5568–5575.

[14] M. D. L. R. Peralta, U. Pal, R. S. Zeferino, *ACS Appl. Mater. Interfaces* 2012, **4**, 4807–4816.

[15] Q. Deng, X. Duan, D. H. L. Ng, H. Tang, Y. Yang, M. Kong, Z. Wu, W. Cai, G. Wang, *ACS Appl. Mater. Interfaces* 2012, **4**, 6030−6037.

[16] N. S. Han, D. Kim, J. W. Lee, J. Kim, H. S. Shim, Y. Lee, D. Lee, J. K. Song, *ACS Appl. Mater. Interfaces* 2016, **8**, 1067–1072.

[17] C. Eley, T. Li, F. Liao, S. M. Fairclough, J. M. Smith, G. Smith, S. C. E. Tsang, *Angew. Chem.* 2014, **53**, 7838–7842.

[18] F. Shen, W. Que, Y. He, Y. Yuan, X. Yin, G. Wang, *ACS Appl. Mater. Interfaces* 2012, **4**, 4087−4092.

[19] A. Kargar, Y. Jing, S. J. Kim, C. T. Riley, X. Pan, D. Wang, *ACS Nano* 2013, **7**, 11112–11120.

[20] Z. Zhang, C. Shao, X. Li, C. Wang, M. Zhang, Y. Liu, *ACS Appl. Mater. Interfaces* 2010, **2**, 2915–2923.

[21] Y. Tang, P. Traveerungroj, H. L. Tan, P. Wang, R. Amal, Y. H. Ng, *J. Mater. Chem. A* 2015, **3**, 19582–19587.

[22] T. M. Gür, S. F. Bent, F. B. Prinz, *J. Phys. Chem. C* 2014, **118**, 21301−21315.

[23] S. A. Vanalakar, S. S. Mali, R. C. Pawar, N. L. Tarwal, A. V. Moholkar, J. H. Kim, P. S. Patil, *J. Appl. Phys.* 2012, **112**, 044302.

[24] S.A. Vanalakar, R.C. Pawar, M.P. Suryawanshi, S.S. Mali, D.S. Dalavi, A.V. Moholkar, K.U. Sim, Y.B. Kown , J.H. Kim, P.S. Patil, *Mater. Lett.* 2011, **65**, 548–551.

[25] X. Wang, K. Maeda, A. Thomas, K. Takanabe, G. Xin, J. M. Carlsson, K. Domen, M. Antonietti, *Nat. Mater.* 2009, **8**, 76–80.

[26] X. Du, G. Zou, Z. Wang, X. Wang, *Nanoscale* 2015, **7**, 8701–8706.

[27] S. C. Yan, Z. S. Li, Z. G. Zou, *Langmuir* 2009, **25**, 10397–10401.

[28] S. C. Yan, Z. S. Li, Z. G. Zou, *Langmuir* 2010, **26**, 3894–3901.

[29] Z. Huang, F. Li, B. Chen, G. Yuan, *ChemSusChem* 2016, **9**, 1–8.

[30] Q. Han, B. Wang, J. Gao, Z. Cheng, Y. Zhao, Z. Zhang, L. Qu, *ACS Nano* 2016, **10**, 2745–2751.

[31] W. Liu, M. Wang, C. Xu, S. Chen, *Chemical Engineering Journal* 2012, **209**, 386–393.

[32] Y. Wang, R. Shi, J. Lin, Y. Zhu, *Energy Environ. Sci.* 2011, **4**, 2922–2929.

[33] W. Yu, D. Xu, T. Peng, *J. Mater. Chem. A* 2015, **3**, 19936–19947.

[34] J. X. Sun, Y. P. Yuan, L. G. Qiu, X. Jiang, A. J. Xie, Y. H. Shen, J. F. Zhu, *Dalton Trans.* 2012, **41**, 6756–6763.

[35] Y. Bu, Z. Chen, *RSC Adv.* 2014, **4**, 45397–45406.

[36] J. Zhou, M. Zhang, Y. Zhu, *Phys. Chem. Chem. Phys.* 2014, **16**, 17627−17633.

[37] S. Kumar, A. Baruah, S. Tonda, B. Kumar, V. Shanker, B. Sreedhar, *Nanoscale* 2014, **6**, 4830–4842.

[38] D. Chen, K. Wang, D. Xiang, R. Zong, W. Yao, Y. Zhu, *Applied Catalysis B: Environmental* 2014, **147**, 554–561.

[39] Y. Zhu, M. Li, Y. Liu, T. Ren, Z. Yuan, *J. Phys. Chem. C* 2014, **118**, 10963−10971.

[40] R. C. Pawar, Y. son, J. Kim, S. H. Ahn, C. S. Lee, *Current Applied Physics* 2016, **16**, 101-108.

[41] P. Fageria, R. Nazir, S. Gangopadhyay, H. C. Barshiliac, S. Pande, *RSC Adv.* 2015, **5**, 80397–80409.

[42] P. Y. Kuang, Y. Z. Su, G. F. Chen, Z. Luo, S. Y. Xing, Nan Li, Z. Q. Liu, *Appl. Surf. Sci.* 2015, **358**, 296–303.

[43] Y. Tak, K. Yong, *J. Phys. Chem. B* 2005, **109**, 19263–19269.

[44] X. M. Liu, Y. C. Zhou, *Journal of Crystal Growth* 2004, **270**, 527–534.

[45] L. E. Greene, M. Law, D. H. Tan, M. Montano, J. Goldberger, G. Somorjai, P. Yang, *Nano Lett.* 2005, **5**, 1231−1236.

[46] Z. Khan, T. R. Chetia, A. K. Vardhaman, D. Barpuzary, C. V. Sastri, M. Qureshi, *RSC Advances* 2012, **2**, 12122–12128.

[47] J. Bian, J. Li, S. Kalytchuk, Y. Wang, Q. Li, T. C. Lau, T. A. Niehaus, A. L. Rogach, R. Zhang, *ChemPhysChem* 2015, **16**, 954–959.

[48] J. Bian, Q. Li, C. Huang, J. Li, Y. Guo, M. Zaw, R. Zhang, *Nano Energy* 2015, **15**, 353–361.

[49] C. C. Li, X. M. Yin, Q. H. Li, T. H. Wang, *CrystEngComm* 2011, **13**, 1557–1563.

[50] Y. Peng, S. Qin, W. Wang, A. Xu, *CrystEngComm* 2013, **15**, 6518–6525.

[51] D. R. Kumar, D. Manoj, J. Santhanalakshmi, *RSC Adv.* 2014, **4**, 8943–8952.

[52] Z. Zhou, Y. Shen, Y. Li, A. Liu, S. Liu, Y. Zhang, *ACS Nano* 2015, **9**, 12480–12487.

[53] H. Yan, H. Yang, *J. Alloy Compd.* 2011, **509**, 26–29.

[54] T. Bora, D. Zoepfl, J. Dutta, *Scientific reports* 2016, **6**, DOI: 10.1038/srep26913.

[55] H. L. Guo, Q. Zhu, X. L. Wu, Y. F. Jiang, X. Xie, A. W. Xu, *Nanoscale* 2015, **7**, 7216–7223

[56] H. Zhang, X. Lv, Y. Li, Y. Wang, J. Li, *ACS Nano* 2010, **4**, 380–386.

[57] M. Nasir, Z. Xi, M. Xing, J. Zhang, F. Chen, B. Tian, S. Bagwasi, *J. Phys. Chem. C* 2013, **117**, 9520−9528.

[58] B. Cai, X. Lv, S. Gan, M. Zhou, W. Ma, T. Wu, F. Li, D. Han, L. Niu, *Nanoscale*, 2013, **5**, 1910–1916.

[59] X. Li, Y. Jiang, W. Cheng, Y. Li, X. Xu, K. Lin, *Nano-Micro Lett.* 2015, **7**, 243–254.

The English in this document has been checked by at least two professional editors, both native speakers of English. For a certificate, please see:

http://www.textcheck.com/certificate/X6KhuS

Table of Contents entry

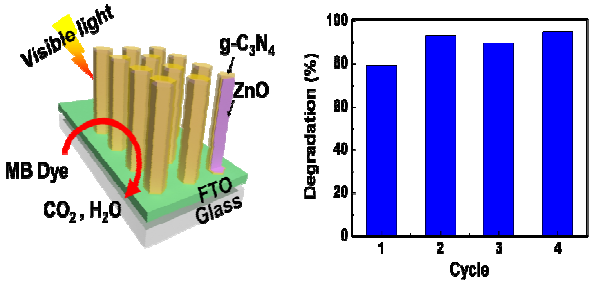

The novelty and the main content of the manuscript

Aligned 1D ZnO/g-C_3N_4 films were fabricated by simple refluxing with thermal vapor condensation for rapid charge separation and recyclable test.

Figure

Figure captions:

Figure 1. Schematic illustration of the fabrication process of zinc oxide (ZnO) with graphitic carbon nitride (g-C_3N_4) films on a fluorine-doped tin oxide (FTO)-coated glass substrate.

Figure 2. Field-emission scanning electron microscope (FE-SEM) images of (a) the top-view and (c) cross-sectional view of the ZnO nanorod film on the FTO-coated substrate, (b) the top-view and (d) cross-sectional view of the 1D ZnO/gC_3N_4 films on the FTO-coated substrate and (e) energy-dispersive X-ray spectrometer (EDS) elemental mapping images of the 1D ZnO/gC_3N_4 films.

Figure 3. (a) Low-magnification transmission electron microscope (TEM) images of the ZnO nanorod film on the FTO-coated glass substrate with the selected area electron diffraction (SAED) pattern shown in the inset, and high-magnification high-resolution transmission electron microscope (HR-TEM) images of the (b) ZnO nanorod film and (c) 1D ZnO/gC_3N_4 films on the FTO-coated substrate.

Figure 4. (a) Fourier transform infrared (FT-IR) spectra of ZnO, g-C_3N_4 and 1D ZnO/gC_3N_4 films, (b) overall X-ray photoelectron spectroscopic (XPS) spectra of 1D ZnO/gC_3N_4 films and (c) high resolution Zn 2p, (d) O 1s, (e) C 1s and (f) N 1s XPS spectra.

Figure 5. (a) A linear potential sweep voltammetry plot of the ZnO nanorod film, g-C_3N_4 films and the 1D ZnO/gC_3N_4 films under visible-light irradiation. (b) Photocurrent response of the ZnO nanorod films, g-C_3N_4 films and the 1D ZnO/gC_3N_4 films under visible-light irradiation. Electrochemical impedance spectroscopy (EIS) Nyquist plots of the ZnO nanorod films, g-C_3N_4 films and the 1D ZnO/gC_3N_4 films (c) in the dark and (d) under visible-light irradiation.

Figure 6. Photostability measurements of the ZnO nanorod films, g-C_3N_4 films and the 1D ZnO/gC_3N_4 films as a function of irradiation time.

Figure 7. (a) Photocatalytic activities of the blank, the ZnO nanorod films, g-C_3N_4 films and the 1D ZnO/gC_3N_4 films toward methylene blue (MB) dye degradation under visible light. (b) Pseudo-first-order kinetic plots for the MB dye degradation. (c) Four successive photocatalytic activity cycles of the 1D ZnO/gC_3N_4 films toward the degradation of MB dye. (d) A plot of the MB dye photodegradation by the 1D ZnO/gC_3N_4 films under visible light in the presence of *tert*-butanol, EDTA-2Na and no scavenger.

Figure 8. Schematic illustration of the separation of photogenerated charge carriers in 1D ZnO/gC_3N_4 films and the proposed mechanism for the MB dye degradation.

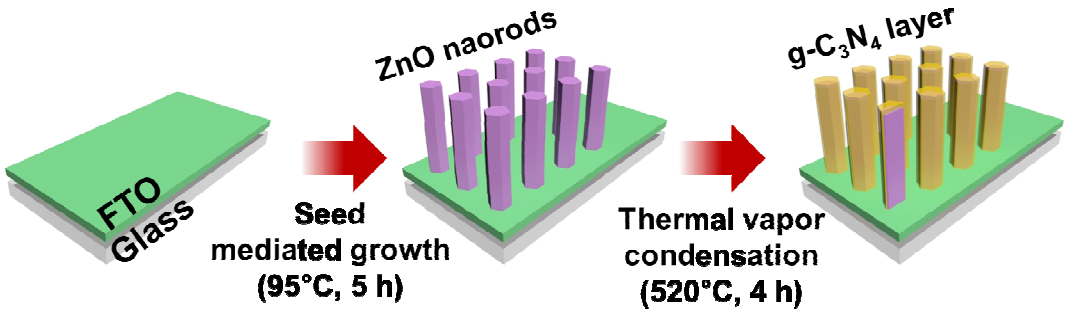

Figure 1.

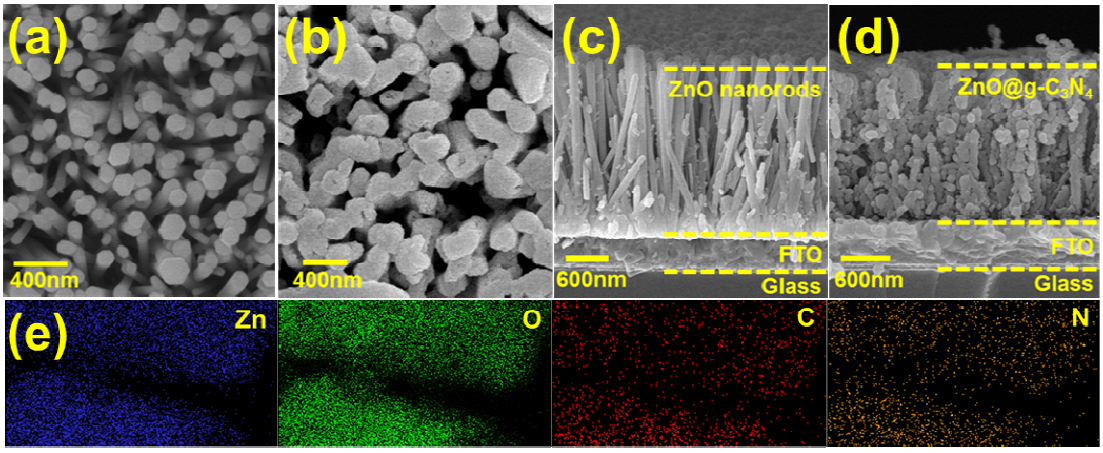

Figure 2. (a)-(e)

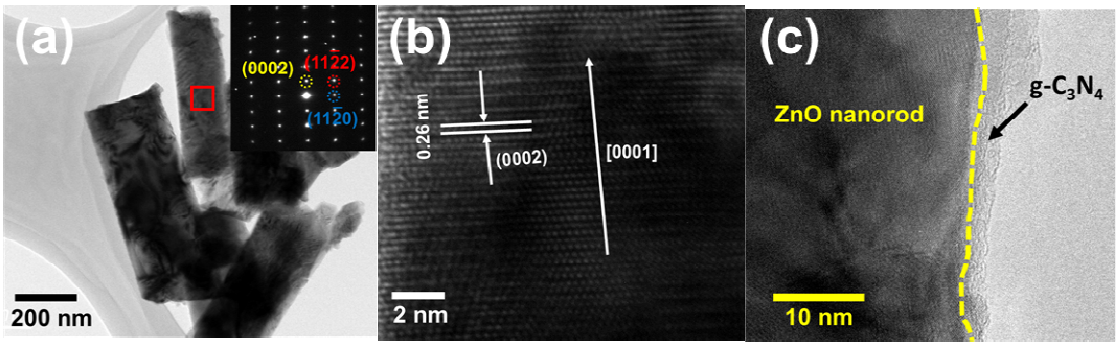

Figure 3. (a)-(c)

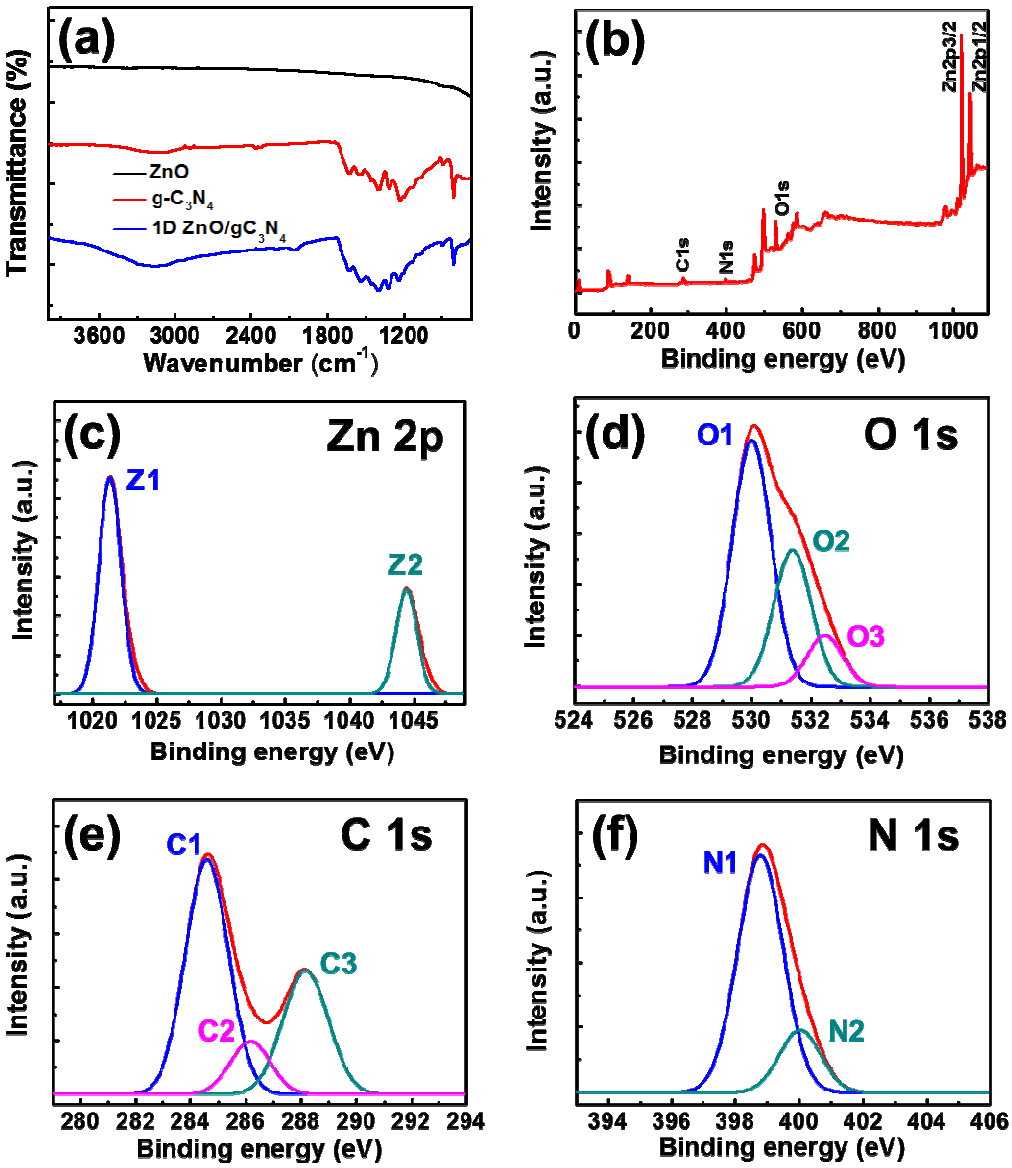

Figure 4. (a)-(f)

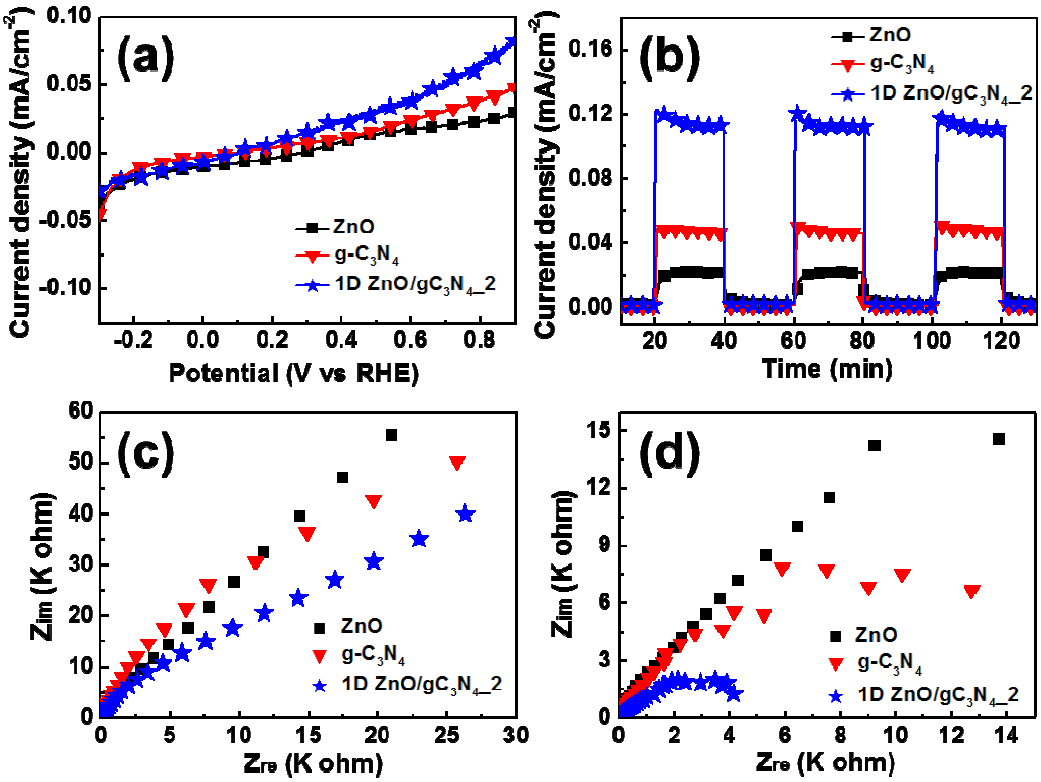

Figure 5. (a)-(d)

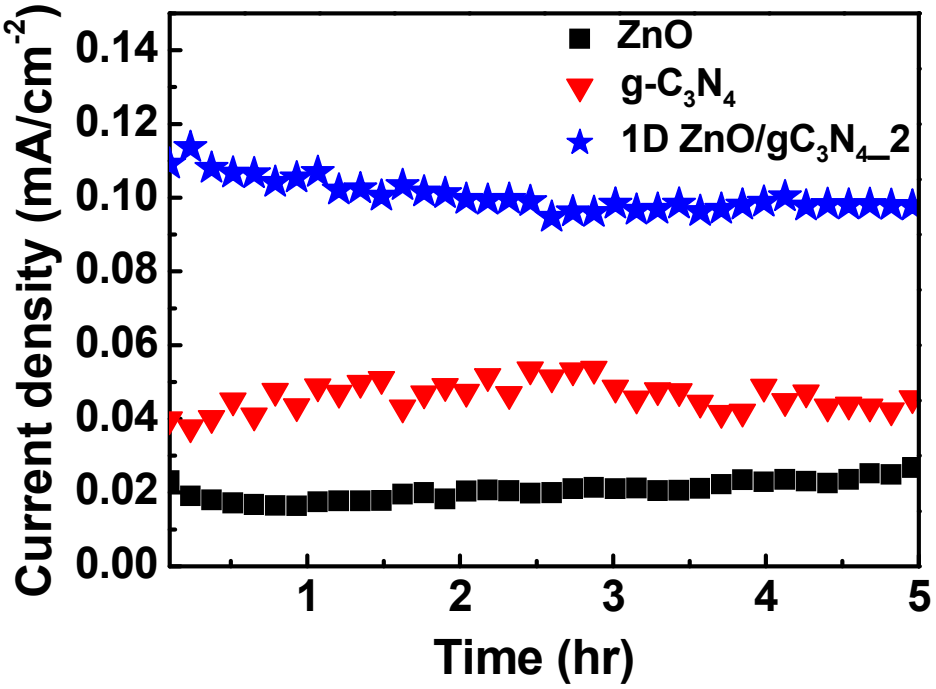

Figure 6.

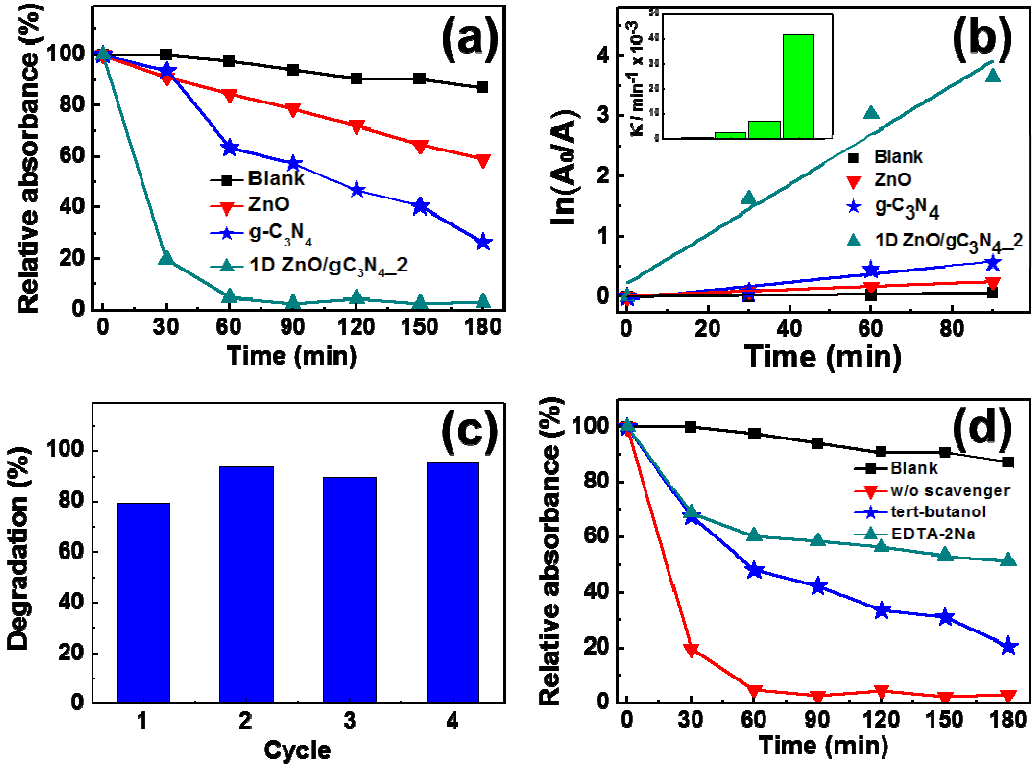

Figure 7. (a)-(d)

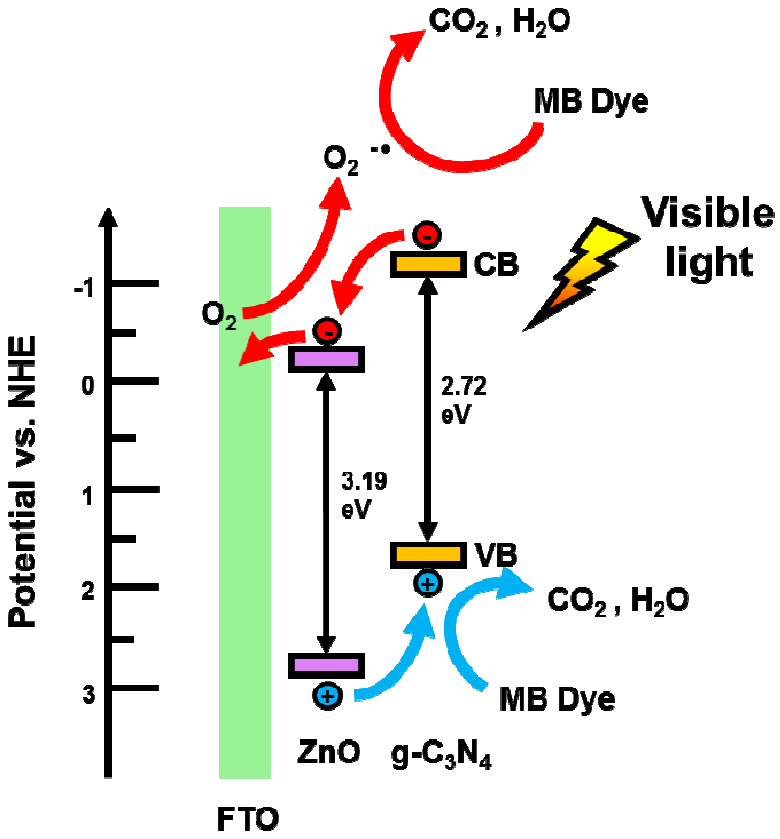

Figure 8.